ACS OMEGA

Open Access

http://pubs.acs.org/journal/acsodf

Article

Synthesis of 2D $PtSe_2$ Nanolayers on Glass Substrates and Their Integration in Near-Infrared Light Shutters

Nikolay Minev, Krastyo Buchkov, Nadia Todorova, Rosen Todorov, Vladimira Videva, Maria Stefanova, Peter Rafailov, Daniela Karashanova, Hristosko Dikov, Velichka Strijkova, Christos Trapalis, Shiuan Huei Lin, Dimitre Dimitrov, and Vera Marinova*

Cite This: *ACS Omega* 2024, 9, 14874−14886

Read Online

ACCESS | Metrics & More | Article Recommendations | Supporting Information

ABSTRACT: $PtSe_2$ has asserted its key role among the emerging 2D transition metal dichalcogenides, however, its simplified growth process with controlled number of layers, high crystalline quality, and on inexpensive substrates is still challenging. Here, we report the synthesis details of $PtSe_2$ layers on soda lime glass substrates by selenization of predeposited Pt layers using the thermally assisted conversion method at atmospheric pressure. $PtSe_2$ syntheses are confirmed by X-ray photoelectron spectroscopy and Raman analysis. The layers were further investigated with transmission electron microscopy and optical ellipsometry, revealing the thickness and its dependence on the metal precursor sputtering time. Finally, the integration of $PtSe_2$ as transparent conductive layers in polymer-dispersed liquid crystal structures operating as near-infrared light shutters is demonstrated and device performance is discussed. The proposed simple and inexpensive synthesis approach opens up new directions toward $PtSe_2$ potential technological applications, including ITO-free optoelectronics.

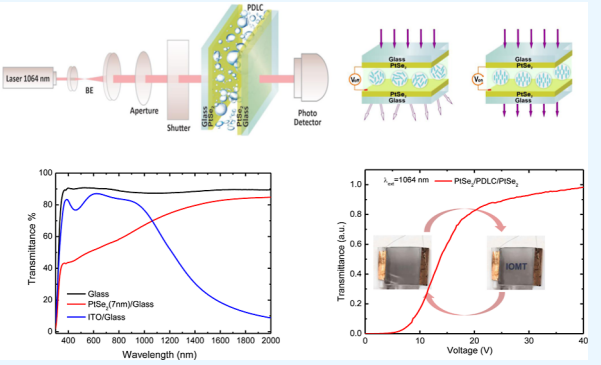

1. INTRODUCTION

Transition metal dichalcogenides (TMDCs) are a new growing family of atomically thin materials, represented by the general chemical formula MX_2 (M = transition metal and X = S, Se, or Te). TMDCs are layered in nature, having strong covalent bonds between the atoms of a single layer while the interaction of adjacent layers is mediated by weak van der Waals forces.[1,2] As a consequence, TMDC monolayers can be easily produced via mechanical exfoliation. In addition, they possess tunable band gaps in the range of 1−2 eV (transition to direct band gap as the number of layers goes down), making them valuable in a wide range of heterostructure-based electronic/optoelectronic devices and catalysts.[3] In terms of electrical properties, the family of ultrathin (one to few atomic layers) TMDCs vary from semiconductors to superconductors.[4] Precise tuning of the band gap can be done by controlling the number of layers or using strain in some cases. In this regard, TMDCs demonstrate great potentials for sensing and energy storage, photovoltaics, photodetectors, field-effect transistors, catalysts for solar-driven hydrogen evolution reaction, in biotechnology, spintronics, etc.[5]

Platinum diselenide ($PtSe_2$) is a noticeable member of group-10 of the TMDC family that has attracted great attention due to its air stability, excellent photoelectric and electrical properties, strong catalytic effect, and potential use in high-performance photodetectors, energy harvesting, and solar cells, just to mention a few.[6] $PtSe_2$ demonstrates the most prominent atomic-layer-dependent electronic behavior of "semiconductor-to-semimetal" transition when going from the monolayer to bulk form. In the monolayer form, it is a semiconductor with a band gap of 1.2 eV[7,8] while the bulk $PtSe_2$ is a semimetal with almost zero band gap. The semimetal-to-metal transition is due to the strong interaction between the interlayer chalcogen atoms (Se), making the out-of-plane valence bond broader and overlapping, leading to its increased metallic properties even with a small number of layers.[1,9] It has been reported that semiconductor-to-semimetal transition in $PtSe_2$ can also be induced by near-atomic defects and Se vacancies.[10] Hence, $PtSe_2$ has found applications as high-performance gas sensors with extremely short response and recovery times in renewable energy devices for direct solar-to-hydrogen production and demonstrates superior electrocatalytic activity for the hydrogen evolution reaction.[11] Recently, $PtSe_2$-based reusable electronic tattoos as advanced building blocks of future wearable bioelectronics for monitor-

Received: October 19, 2023
Revised: March 2, 2024
Accepted: March 6, 2024
Published: March 22, 2024

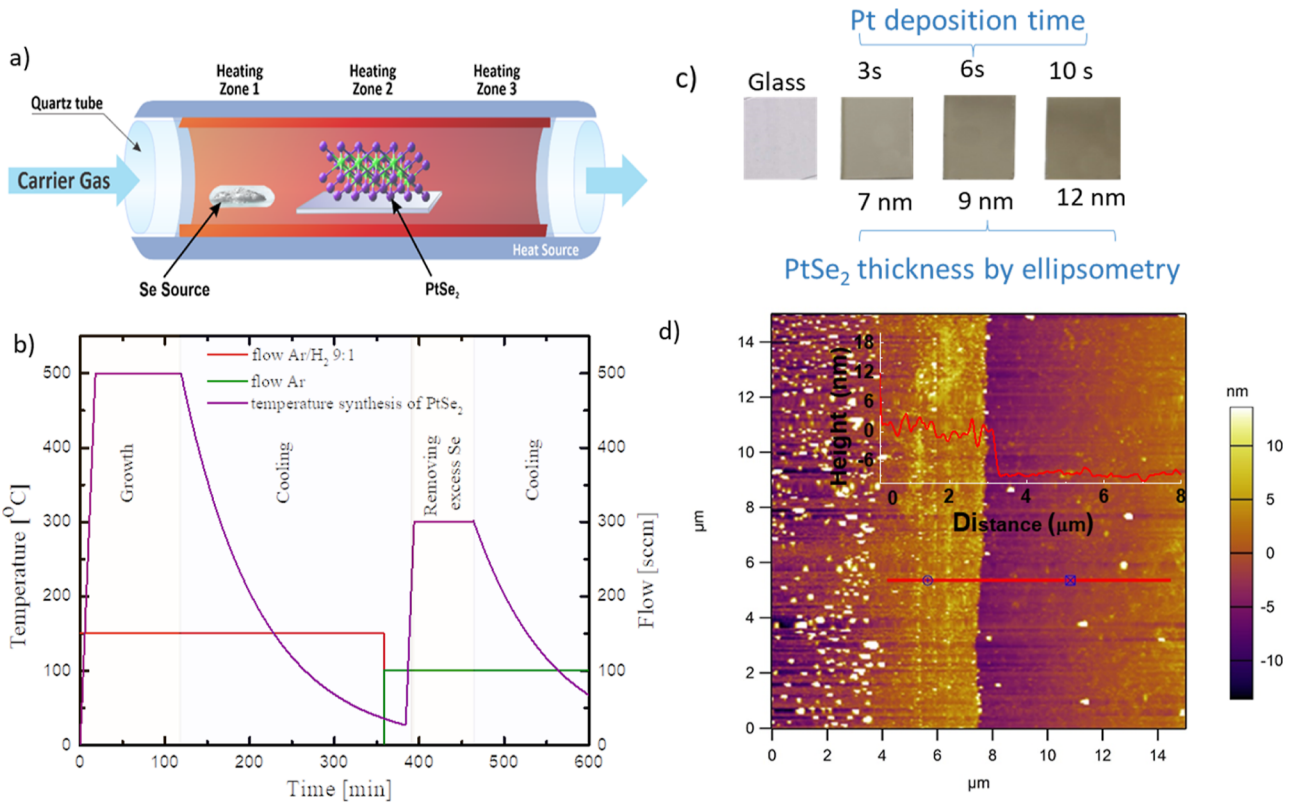

Figure 1. (a) Schematic diagram of three-zone atmospheric pressure CVD (TAC) system; (b) temperature, time, and flow diagrams of the growth process; (c) photographs of synthesized $PtSe_2$ layers on glass substrates; and (d) AFM image of $PtSe_2$ (6 s deposition time of the Pt layer) with the height profile across the straight solid red line (the scale bar is 2 μm) indicating the layer thickness of ~9.5 nm.

ing human physiological vital signs with diverse bioelectronics application have been demonstrated.[12]

Moreover, the extremely high sensitivity of $PtSe_2$ at the near-infrared spectral range has proved it to be an advanced material for lowering energy consumption by modulating the transmission of near-infrared light of solar irradiation.[13−17] This may have a big impact, for example, in smart windows' design, which can selectively modulate the light transmittance and color on demand. Therefore, the integration of $PtSe_2$ as a supporting transparent conductive layer in liquid crystal(LC)-based devices opens up a new road for so-called ITO-free near-infrared light shutters, displays, and a variety of switchable optical devices. Furthermore, $PtSe_2$ is stable in air, which brings further benefits in device applications.

In this aspect, controlled large-scale synthesis of $PtSe_2$ layers on inexpensive optically transparent substrates is an important step toward future practical integration. Chemical vapor deposition (CVD) and particularly its derivative thermally assisted conversion (TAC) method have been proven as a simple, precise, and reliable way to obtain wafer-scale 2D $PtSe_2$ films. The TAC process allows synthesizing large-scale $PtSe_2$ by direct selenization of Pt where the lateral size and thickness of the $PtSe_2$ film can be controlled by modulating the thickness of the predeposited Pt film and substrate size, respectively.[18−20] Wang et al. in 2015 first fabricated a single crystal monolayer $PtSe_2$ by direct selenization of the Pt(111) substrate.[9] To date, the majority of the reported $PtSe_2$ layers were synthesized by direct selenization of predeposited Pt thin layers via the TAC route.[21,22] Although large-area $PtSe_2$ thin layers can be synthesized by direct selenization through the TAC approach, it is still challenging to obtain $PtSe_2$ layers thin enough, below which the "semiconductor-to-semimetal" transition is expected to occur.[23] Also, an important concern is the substrate selection, for example Si,[24−26] Si/SiO_2,[27,28] fused quartz,[29−31] and sapphire[32] are the most used, however, they are rather expensive. Besides these conventional substrates, the 2D $PtSe_2$ film has been successfully grown on gallium nitride,[33] as well as on NaCl which after dissolution led to free-standing $PtSe_2$ films.[34] Importantly, $PtSe_2$ can be grown at a relatively low temperature (400 °C)[12,35] in comparison to other TMDCs[36,37] or other layered 2D materials,[38−40] which enables it to be synthesized on a variety of low-temperature-resistant substrates including flexible[41] as well as compatible with those used in back-end-of-line requiring deposition as low as 450 °C.[42] The synthesis performed at 400 °C by TAC represents a breakthrough for the direct integration of 2D $PtSe_2$ with silicon (Si) technology. Recently, we reported on the use of transparent low-cost soda lime glass substrates as a suitable alternative for growth of $PtSe_2$ coatings[43] with emphasis on their antibacterial properties. In the present work, a comprehensive investigation of the $PtSe_2$ coatings deposited on soda lime glass concerning their physicochemical properties is conducted.

This work demonstrates an efficient synthesis of $PtSe_2$ on a glass substrate at atmospheric pressure that enables inexpensive production of large area $PtSe_2$. To the best of our knowledge, this is the first report about the synthesis of 2D $PtSe_2$ on glass substrates using the atmospheric pressure CVD (TAC) method. Moreover, the prepared $PtSe_2$ was integrated as a conductive layer in polymer-dispersed liquid crystal (PDLC) structures and tested as a near-infrared optical switchable device. The proposed approach can be potentially

https://doi.org/10.1021/acsomega.3c08235
ACS Omega 2024, 9, 14874−14886

used for other TMDC members and accelerate their further applications.

2. EXPERIMENTAL SECTION

2.1. Synthesis of $PtSe_2$ Layers. $PtSe_2$ layers were synthesized via the TAC method with the following steps and experimental conditions: first, the substrates were cleaned in 1% (vv) Hellmanex solution followed by sonication in isopropanol for 5 min. The Pt metal layer was deposited by magnetron sputtering onto soda lime glass (Knittel Glasbearbeitungs GmbH) substrates followed by subsequent selenization. For this purpose, 1 g of high purity selenium (Se) was placed upstream at the heating zone 1 (280 °C) while the predeposited Pt layers were placed in the heating zone 2 (500 °C) of a horizontal quartz tube CVD reactor as depicted in Figure 1a. The temperature of zone 1 was chosen to produce sufficient selenium vapor and that of zone 2 was chosen to ensure conversion of the initial Pt into $PtSe_2$. The temperature in the zone 3 was set to 530 °C to counter heat losses and maintain a uniform temperature gradient between zones 2 and 3. Prior to selenization, the residual oxygen was removed from the system by flowing a 150 sccm gas mixture Ar/H_2 (9:1) for 20 min. Immediately after that, the heaters were turned on with heating rates 16.5 °C/min (heating zone 1) and 27.8 °C/min (heating zones 2 and 3). Heating time (heating rate) of 18 min to reach the synthesis temperature was chosen in order to ensure optimal heat transfer between the furnace heaters and the substrate. In addition, the slow heating rate ensures that all zones have enough time to reach their temperature set points simultaneously. The dwell time was set to 2 h to ensure that the entire initial Pt is converted into $PtSe_2$. The $PtSe_2$ samples were allowed to cool unassisted to room temperature. Finally, the samples were heated again to 300 °C under constant 150 sccm Ar flow for 30 min to remove any excess of Se.[9] The overall temperature, time, and flow diagrams are presented in Figure 1b.

Three sets of $PtSe_2$ samples were prepared using Pt sputtering times of 3, 6, and 10 s, respectively, on a glass substrate. In addition, for ellipsometry measurements the same set of $PtSe_2$ samples were prepared on the Si(100) substrate. Later, based on ellipsometry, the thicknesses of the $PtSe_2$ layers were estimated to 7, 9 and 12 nm, respectively, and the samples were tagged with respect to the thicknesses, namely, $PtSe_2$-7, $PtSe_2$-9, and $PtSe_2$-12 nm Figure 1c.

2.2. Characterization Techniques. The surface chemical composition of the samples and the valence state of the elements were investigated by X-ray photoelectron spectroscopy (XPS). The wide survey scan and high-resolution spectra of Pt, Se, and Na regions were obtained using an ultrahigh vacuum VG EXCALAB 210 electron spectrometer with an AlKα ($h\nu$ = 1486.6 eV) radiation source. In order to compensate the surface charging effect, the C 1s peak at 284.8 eV related to adventitious carbon was used for calibration of the spectra.

Atomic force microscopy (AFM) analysis (MFP-3D, Asylum Research, Oxford Instruments) was carried out to evaluate the surface morphology and height profile. The AFM image of $PtSe_2$ (9.5 nm) with the corresponding height profile across the solid red line (the scale bar 2 μm), showing similar thickness to that of ellipsometry analysis discussed later on, is presented in Figure 1d.

The morphology of the $PtSe_2$ layers was examined via scanning electron microscopy (SEM) using an FEI Quanta Inspect instrument with a secondary detector and tungsten filament operating at 25 kV. Prior to the analysis, a Au layer was applied on the material surface through a standard sputtering procedure. The images of $PtSe_2$ layers on glass substrates reveal the formation of a polycrystalline layer for all Pt deposition times (Supporting Information, S1).

The Raman spectra were measured using a 514 nm laser source for the excitation. Raman analysis was performed in backscattering geometry on a HORIBA Jobin Yvon Labram HR visible spectrometer (HORIBA Ltd., Kyoto, Japan) equipped with a Peltier-cooled CCD detector. The laser beam was focused on a spot of approximately 2 μm in diameter on the sample surface by using microscope optics with an objective of 100× magnification.

The microstructure of the Pt layers after selenization was examined by transmission electron microscopy (TEM). For this purpose, the layers were separated from the glass substrates by mechanical exfoliation or cleavage of a few monolayers with thermal tape and then transferred onto standard copper grids covered with amorphous carbon membranes. The study was carried out using a high-resolution transmission electron microscope JEOL JEM 2100 at a 200 kV accelerating voltage. The phase composition of the layers was determined by the selected area electron diffraction and high-resolution TEM (HRTEM) modes. For the phase identification, Match software, Version 3.13 (Crystal Impact GbR, Bonn, Germany), supplied with the crystallography open database (COD) was used.

A UV−vis phase-modulated spectroscopic ellipsometric platform UVISEL2 (HORIBA Jobin Yvon) was used to measure the spectra of quantities I_s and I_c, related to ellipsometric angles ψ and Δ by the following equations: $I_s = \sin 2\Psi \cdot \sin\Delta$ and $I_c = \sin 2\psi \cdot \cos\Delta$. The measurements were conducted in the spectral range of 0.6−6 eV at incident angles of −50, 60, and 70°, respectively.

The optical transmittance spectra in the wavelength range of 200−2000 nm were measured at room temperature using an UV−vis−near-infrared spectrophotometer Cary 5E.

2.3. $PtSe_2$-Based PDLC Structure Fabrication. For assembling PDLC structures based on $PtSe_2$ layers, first an empty cell was arranged by gluing two $PtSe_2$/glass substrates ($PtSe_2$ layers facing each other) separated with 12 μm Mylar spacers between them. Next, the LC/monomer mixture was prepared using LC E7 (Merck, n_0 = 1.521 and n_e = 1.72) and photocurable adhesive polymer matrix (NOA65, Norland, Cranbury, NJ, USA, n = 1.524) in a 30:70 wt % ratio. The mixture was injected into the empty cell by the capillary method. Finally, the cell was exposed with UV light (UV −365 nm for 15 min) to polymerize NOA65. As a result, randomly dispersed LC droplets were formed within the transparent polymer matrix. To measure the electro-optical modulation characteristics, a $PtSe_2$-based PDLC structure was placed at optical setup between a collimator and optical lenses. Cobolt Rumba laser emitting at λ = 1064 nm was used to probe the changes of transmitted intensity of the $PtSe_2$-based PDLC structure under different amplitudes of the applied voltage. The power of the transmitted beam was monitored by a power meter. In addition, a reference PDLC structure, based on commercially available ITO layers, following the same fabrication procedure and thickness of the cell has been prepared for comparison.

https://doi.org/10.1021/acsomega.3c08235
ACS Omega 2024, 9, 14874−14886

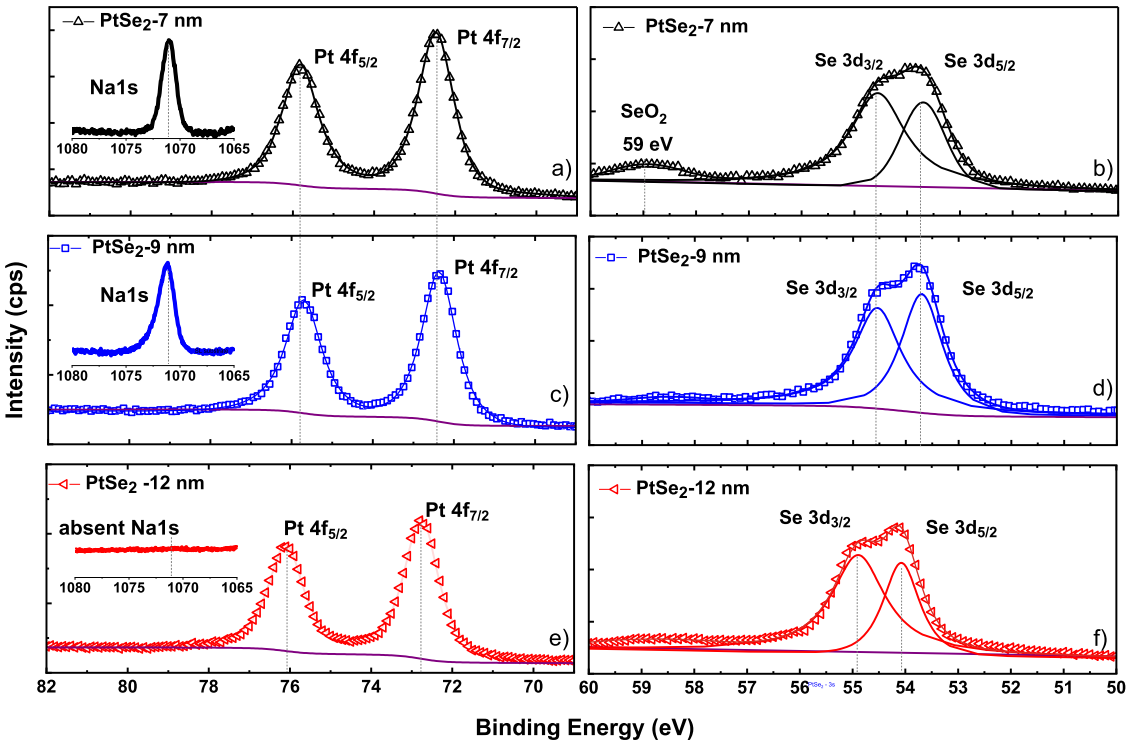

Figure 2. (a–f) XPS spectra of Pt 4f, Se 3d, and the Na 1s (insets) for the $PtSe_2$-7, $PtSe_2$-9, and $PtSe_2$-12 nm layers.

3. RESULTS AND DISCUSSION

3.1. Surface Chemical Composition Analysis. The chemical state, bonding of elements, and stoichiometry of the $PtSe_2$ layers are estimated from the XPS analysis and the spectra are presented in Figure 2. In general, the results evidenced effective TAC of the predeposited Pt to Pt^{4+} and formation of $PtSe_2$ during the selenization process. Specifically, the identified binding energies and oxidation states of the Pt-related peaks (doublets Pt^{4+}-$4f_{5/2}$ and Pt^{4+}-$4f_{7/2}$) and the Se-related peaks (doublets Se^{2-}-$3d_{3/2}$ and Se^{2-}-$3d_{5/2}$) are consistent with those reported in the literature for $PtSe_2$.[1,24,44] In the Pt 4f spectra, a signal for elemental Pt at ~71 eV[1,25,45] was not found indicating that the entire spectrum can be assigned to Pt^{4+} that corresponds to $PtSe_2$. For all samples, the Se 3d spectra contain Se^{2-} ($3d_{3/2}$ and $3d_{5/2}$) ascribed to $PtSe_2$ while for the sample $PtSe_2$-7 nm Se in the form of SeO_2 (at ~59 eV) is present[25,46] that can be explained with the bonding of Se with O from the substrate. Notably, the peak disappeared with the increase of the Pt-deposition time and the consequent increase in $PtSe_2$ thickness and substrate coverage. The shift of the Pt 4f and Se 3d to higher binding energies in the line of $PtSe_2$-7, $PtSe_2$-9, and $PtSe_2$-12 nm can also be related to the increasing thickness of the $PtSe_2$ layers as a similar phenomenon is reported in the literature.[45] The obtained Se/Pt stoichiometric ratios for the samples $PtSe_2$-7, $PtSe_2$-9, and $PtSe_2$-12 nm are ~2.5, 2.2, and 1.9, respectively, marking the stoichiometry level variations depending on the thickness under the same TAC selenization conditions.[47,48] The presence of Se vacancies (Se/Pt < 2) are known to improve the light absorption in the mid-infrared region,[24] as well as the catalytic activity due to local charge trapping.[49] At this point, it could be mentioned that our recent study on the photocatalytic antibacterial activity already evidenced superior behavior of $PtSe_2$ with a low Se/Pt ratio,[43] while for incorporation in near-infrared light shutter devices that is aimed in the present work, the sample with optimum balance of the Se/Pt ratio and thickness would be considered as the best candidate.

It is worth mentioning that there are several reports on addition of various halide salts (NaCl, KBr, KI, etc.) to the metal precursor ($PtCl_2$, WO_3, MoO_2, etc.) during the synthesis process in order to (i) lower the melting point, (ii) improve the nucleation process, and (iii) promote the lateral growth of the TMDC.[50,51] The important role of the sodium ions (Na^+) on the atmospheric pressure CVD synthesis of TMDCs and their heterostructures have been experimentally demonstrated.[52] Besides, it is well-known that the soda lime glass substrate acts as a source of Na^+ which due to their high mobility diffuse in thin coatings such as TiO_2, FeS_2, $Cu(In,Ga)Se_2$, etc. during their deposition.[53−55] The Na^+ are reported to occupy metal sites creating defects[56] with the effect of the Na^+ on the films' properties to be either advantageous[57] or disadvantageous[58] depending on their abundance. To control or inhibit the Na^+ diffusion in the films, suitable diffusion barrier under-layers such as Mo[55] or SiO_2[57−59] have been employed when necessary. In this work, the detected Na^+ ions originate from the soda lime glass used as a substrate for $PtSe_2$ growth. It is observed that the Na 1s signal intensity (XPS spectra in the insets) is significantly decreased for the sample $PtSe_2$-12 nm. The outcome can be associated with the increased coverage of the glass substrate and the higher thickness of this $PtSe_2$ layer impeding the Na^+ migration to the surface.

3.2. Spectroscopic Ellipsometry. The refractive index and extinction coefficient are fundamental properties, which not only determine the optical response of the media but also directly connect the complex permittivity and dielectric constant. To calculate the optical constants, we used a model of a single semiconductor film with a rough overlayer on an absorbing substrate (Si-wafer). Its validity was

https://doi.org/10.1021/acsomega.3c08235
ACS Omega 2024, 9, 14874−14886

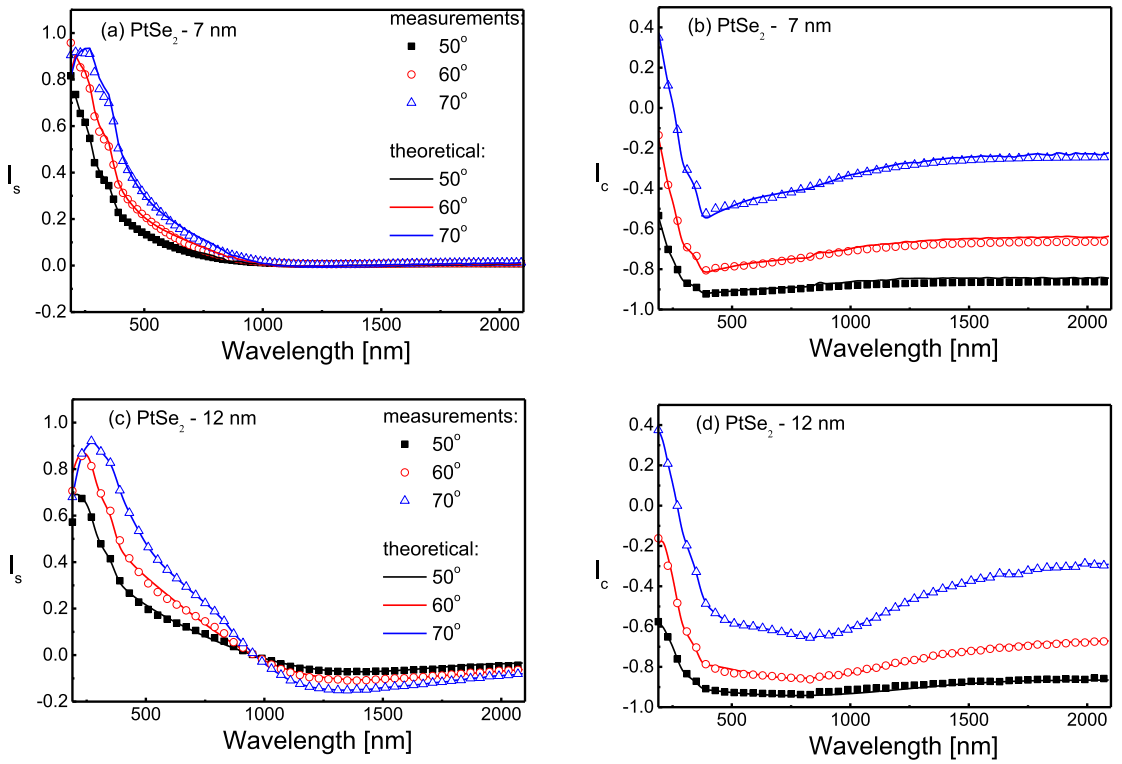

Figure 3. (a–d) Experimental spectra and theoretically calculated values of I_s and I_c for thin $PtSe_2$ layers obtained at Pt sputtering times of 3 and 10 s, which correspond to the thicknesses of 7 and 12 nm, respectively.

determined by calculation of eq 1 of a mean square error function (χ^2), which accounts for the discrepancies between the measured spectra of I_{cmeas} and I_{smeas} and theoretically calculated values for I_{ccalc} and I_{scalc}

$$\chi^2 = \frac{1}{2N - P - 1}\sum_{i=1}^{N}\{[I_{scalc}(h\nu) - I_{smeas}(h\nu)]^2 + [I_{ccalc}(h\nu) - I_{cmeas}(h\nu)]^2\} \quad (1)$$

where N and P are the total number of data points and the number of fitted parameters, respectively.

The theoretical values of $I_{scalc.}$ and $I_{ccalc.}$ are calculated from the relationship between the ellipsometric angles Ψ and Δ and the optical parameters (complex refractive index or permittivity) in the case of a thin film (see Supporting Information, S2). The influence of the surface roughness of the thin films is accounted for by addition of a surface layer, consisting of 50% chalcogenide material and 50% air.

The Tauc–Lorentz oscillator model was applied for description of the complex permittivity, $\hat{\varepsilon} = \varepsilon_1 + \varepsilon_2$, and applied for determination of the optical constants of thin $PtSe_2$ films from other authors.[48,60,61] The model proposed from Jellison and Modine[62] is a combination of the Tauc law,[63] which describes the spectral dependence of the absorption edge in the case of indirect allowed transitions and the Lorentz oscillator model used in the case of the interband transition i.e., electron transition from the valence to conduction band. The model supplies an expression for the imaginary part, ε_2, of the dielectric function if only a single transition is considered.

$$\varepsilon_2 = \frac{AE_0\Gamma(E - E_g)^2}{(E^2 - E_0^2)^2 + \Gamma^2E^2}\cdot\frac{1}{E} \quad \text{for } E > E_g$$
$$\varepsilon_2 = 0 \quad \text{for } E \le E_g \quad (2)$$

where E_g^{opt} is the optical band gap. In the case of the Tauc–Lorentz model, this is the photon energy at which the absorption becomes zero ($\varepsilon_2 = 0$). E_0 is the energy of maximum transition probability or the energy position of the peak of absorption, Γ is the broadening parameter or damping coefficient linked to the full width at half maximum of the absorption peak, and A is the strength of the absorption peak which depends on the optical transition matrix elements.

The real part of the dielectric function was obtained by the Kramers–Kronig integration of ε_2

$$\varepsilon_1 = \varepsilon_\infty + \frac{2}{\pi}P\int_{E_g}^{\infty}\frac{\xi\varepsilon_2(\xi)}{\xi^2 - E^2}\,d\xi \quad (3)$$

The real and imaginary parts, ε_1 and ε_2, of the complex permittivity are related to the refractive index, n, and the extinction coefficient, k, by the following equations

$$n = \sqrt{\frac{\sqrt{\varepsilon_1^2 + \varepsilon_2^2} + \varepsilon_1}{2}} \quad (4a)$$

$$k = \sqrt{\frac{\sqrt{\varepsilon_1^2 + \varepsilon_2^2} - \varepsilon_1}{2}} \quad (4b)$$

The fitting process includes the choice of suitable initial values using published data[48] for dispersion of the refractive index for dispersion parameters E_g, E_0, Γ, A, and film thickness, d, and their upper and lower boundaries. The minimization of

https://doi.org/10.1021/acsomega.3c08235
ACS Omega 2024, 9, 14874–14886

Table 1. Calculated Dispersion Parameters of the $PtSe_2$ Layers

incident angle	d (±0.7) [nm]	ε_∞(±0.2)	E_g^{opt} (±0.02) [eV]	A (±10) [eV]	E_0 (±0.13) [eV]	Γ (±0.20) [eV]
			Pt (3 s)			
50°	6.8	1.29	0.73	65	1.83	2.01
60°	6.9	1.19	0.77	67	1.78	2.10
70°	6.9	1.14	0.75	71	1.74	2.32
			Pt (6 s)			
50°	9.4	2.25	0.64	109	1.64	2.23
60°	8.9	2.39	0.65	114	1.68	2.38
70°	8.5	2.13	0.65	118	1.51	2.14
			Pt (10 s)			
50°	11.3	2.30	0.65	136	1.36	1.85
60°	12.0	2.47	0.64	138	1.41	2.00
70°	12.0	2.52	0.62	146	1.46	2.13

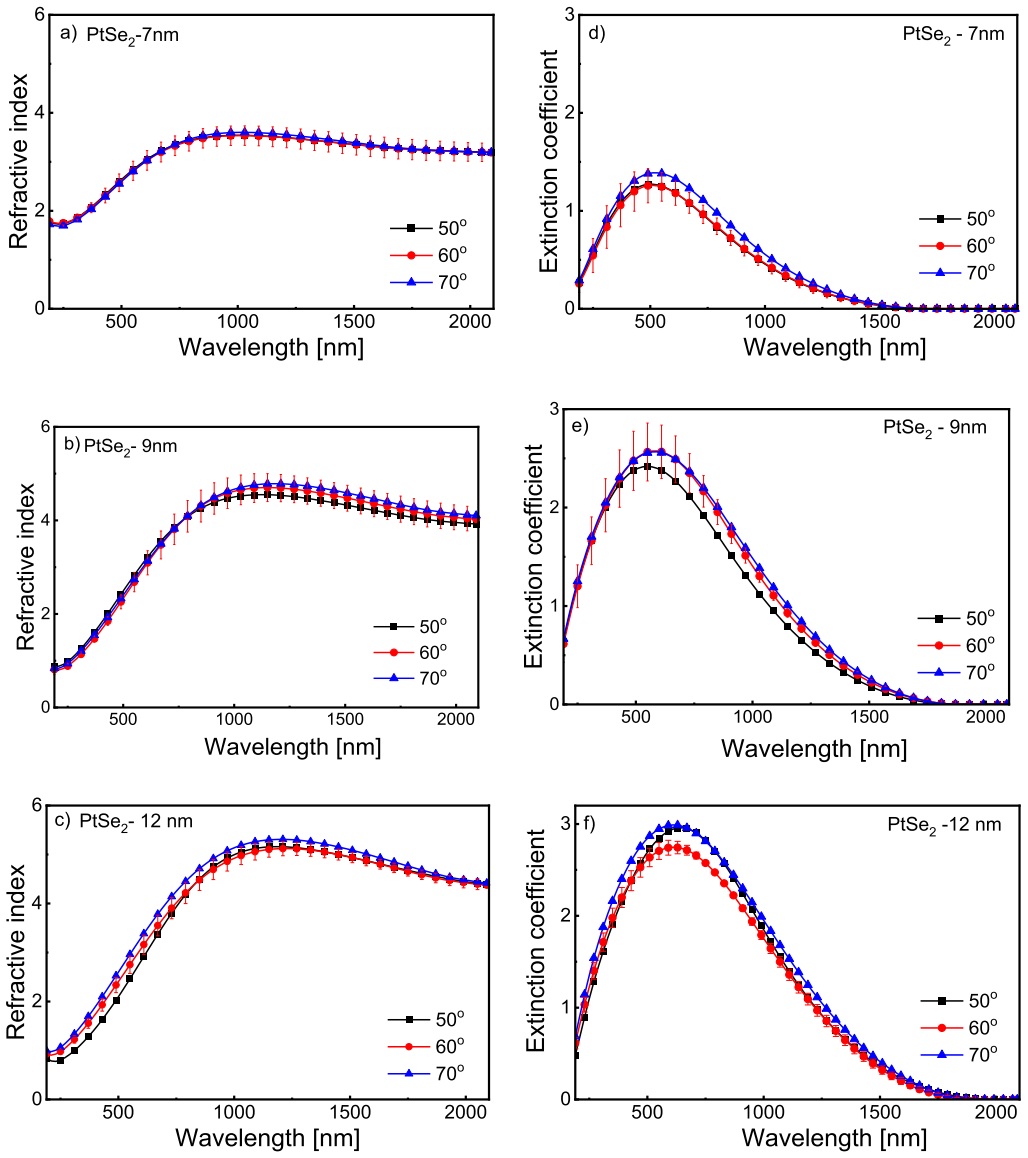

Figure 4. (a–f) Dispersion of the refractive index and extinction coefficient of $PtSe_2$ thin layers with different thicknesses calculated from ellipsometry measurements at incident angles of 50, 60, and 70°.

the χ^2 function was performed in the fitting procedure based on the Levenberg–Marquardt algorithm. The results from the fitting procedures are presented in Figure 3. The calculated values for χ^2, when the single semiconductor layer on the absorbing substrate model was applied, varied from 0.1 to 2.4. A prior experimentally determined presence of a 1.5 nm native SiO_2 layer on the silicon substrate was used in all of the calculations.

https://doi.org/10.1021/acsomega.3c08235
ACS Omega 2024, 9, 14874−14886

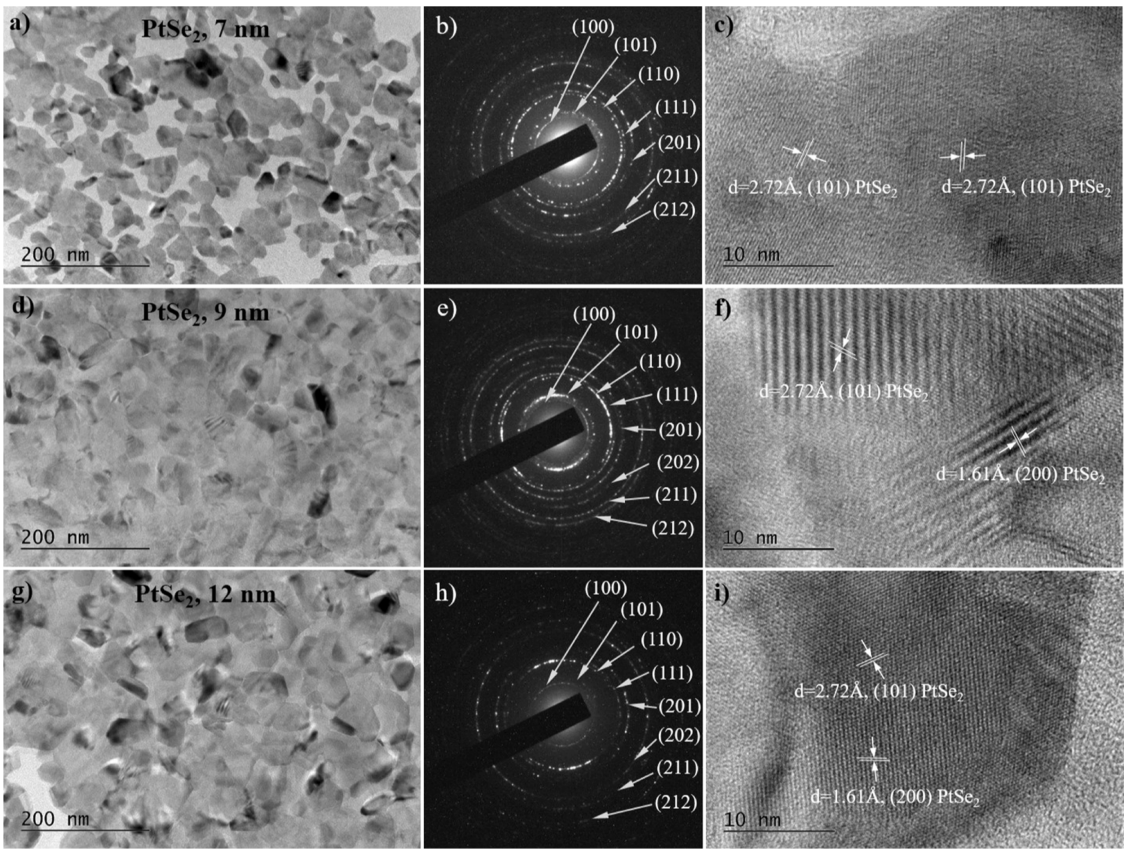

Figure 5. Bright field TEM micrographs at magnification 40,000× of $PtSe_2$-7 nm (a), $PtSe_2$-9 nm (d), and $PtSe_2$-12 nm (g) layers; selected area electron diffraction images of $PtSe_2$-7 nm (b), $PtSe_2$-9 nm (e), and $PtSe_2$-12 nm (h) layers; and HRTEM images of $PtSe_2$-7 nm (c), $PtSe_2$-9 nm (f), and $PtSe_2$-12 nm (i) layers.

The thickness and dispersion parameters (included in eqs 2 and 3), calculated from the ellipsometric measurements, are summarized in Table 1. The calculated values for the thickness d of the thin layers are 12, 9, and 7 nm for Pt sputtering times of 10, 6, and 3 s, respectively. It is seen that the band gap E_g of the thin $PtSe_2$ layers increases from ∼0.65 eV for the layer of 9 nm to ∼0.75 eV for the layer of 7 nm. The extracted values for the optical band gaps hint at the presence of metallic $PtSe_2$. The shrinking of the band gap with increasing thickness is due to strong interlayer interactions, which leads to band splitting or multiplying.[21,48]

The dispersion of the calculated effective refractive index and extinction coefficient are presented in Figure 4a−f. Obviously, within the experimental error, the calculated values of the refractive index and the extinction coefficient do not differ significantly for different incidence angles. More obvious difference was detected when using calculated spectra of I_c and I_s at an angle of incidence of 70°, which may be attributed to the increasing of the surface roughness contribution as the angle of light incidence increases.

The refractive index of few-layer $PtSe_2$ films was found to be strongly thickness-dependent. This can be attributed to the interlayer interaction and its effect on the band structure.[48] As seen, the values of n increase with increasing film thickness in the entire investigated spectral region of 200−2100 nm (Figure 4a−c). The refractive index is characterized by anomalous dispersion at wavelengths shorter than λ < 1000 nm. The anomalous dispersion is likely due to excitons being generated in the $PtSe_2$ layers. Similar behavior has been reported in the dielectric function for other TMDCs.[64,65] Depending on the film thickness, n reaches its maximum values in the spectral region of 1000−1200 nm. The position of the maximum shifts from 1030 to 1190 nm, while the maximal value of n decreases from 5.12 to 3.61 with decreasing film thickness. The refractive index of thin $PtSe_2$ films possesses normal dispersion in the spectral range of 1200−2100 nm. A significant decrease in the values of n with decreasing film thickness is observed in this spectral interval. The decrease in thickness from 12 to 9 nm leads to a decrease in n − from 4.42 to 4.28 at a wavelength of λ = 1700 nm. These values are higher than those obtained in ref 48 for 7.5 nm thick $PtSe_2$ films. Further decreasing the thickness of the thin films to d ∼ 7 nm results in significantly larger changes in the refractive index as the value for n determined for the same wavelength is 3.28.

The calculated values of k show that the extinction coefficient decreases with decreasing film thickness in the whole investigated spectral range (Figure 4d,e). The wide absorption band in the spectral range of 200−1600 nm is observed in the spectra of the extinction coefficient. The maximum position of k shifts to shorter wavelengths with decreasing film thickness, while the values of k at the maximum decrease.

3.3. Transmission Electron Microscopy. TEM analysis was carried out to characterize the microstructure and phase composition of Pt layers after their selenization. The TEM results are presented in Figure 5. Initially, the Pt films were deposited on glass substrates by magnetron sputtering of Pt target at three different times of 3, 6, and 10 s, assuring films

https://doi.org/10.1021/acsomega.3c08235
ACS Omega 2024, 9, 14874−14886

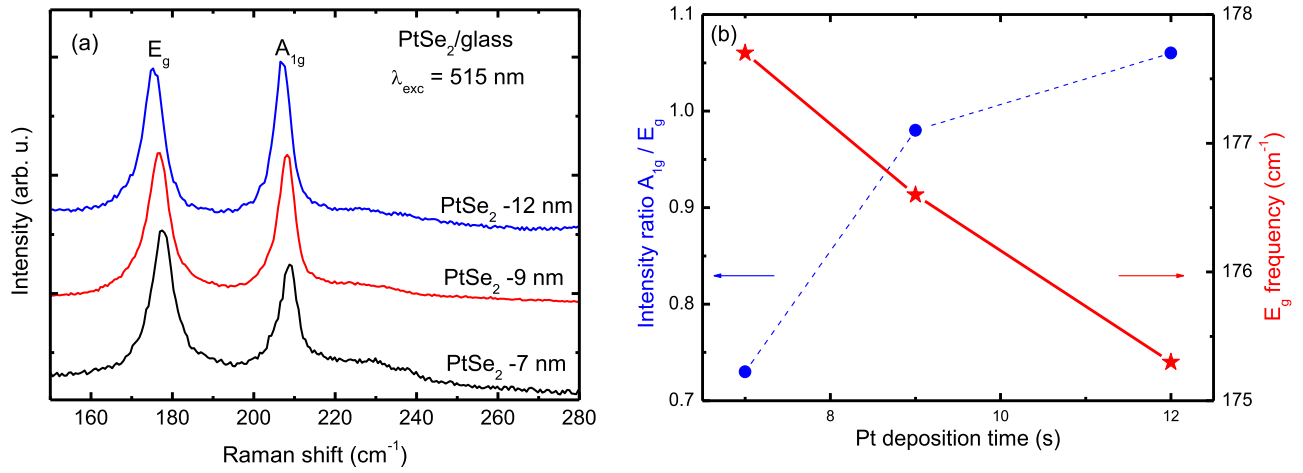

Figure 6. (a) Raman spectra of the three samples with different Pt deposition times labeled by the corresponding $PtSe_2$ thicknesses. The spectra are normalized to the intensity of the E_g line and vertically offset for clarity. (b) Plot of the E_g mode frequency and the A_{1g}/E_g peak intensity ratio vs Pt deposition time which is proportional to the $PtSe_2$ layer thickness.

with three different thicknesses. The amorphous nature of the substrate and the synthesis method applied provoked a polycrystalline film growth, as in other reports, even for some crystalline substrates.[66] The separated Pt grains facilitated the process of selenization at the second step of the experimental procedure as concluded Su et al.[67] and good quality $PtSe_2$ with different thicknesses of 7, 9, and 12 nm, respectively, were produced in the present study. Bright field TEM micrographs of the three samples (Figure 5a,d,g) reveal that the thinnest layer is predominantly discontinuous, while the other two cover the substrate relatively evenly. All three layers possess the typical morphology of a polycrystalline film with randomly oriented crystalline grains, in accordance with the methods of film deposition. The indexing of the diffraction patterns (Figure 5b,e,h) allowed us to determine the phase composition of the layers. A trigonal phase of $PtSe_2$ with the $P\bar{3}m1$ space group and cell parameters a = 3.72400 Å and c = 5.06200 Å (COD entry #96-900-9118), which is also confirmed for the chemical composition of layers' surfaces by XPS analysis, was identified. By measuring the interplanar distances from the HRTEM images (Figure 5c,f,i), the presence of the same phase in the three layers was also determined. It was found that the predominant scattering of the electron beam in these samples was produced by (101) and (200) crystal planes. The established phase composition confirmed the successful implementation of the initial Pt layers' selenization process in the current study.

As can be seen from TEM images, as the thickness of the layer decreases, the number and the size of $PtSe_2$ crystal grains decrease, and in the case of $PtSe_2$-7 nm thickness, the film becomes discontinuous. This indicates that the density of the thin films decreases, resulting in a decrease in the refractive index.

The theoretical calculations and experimental results[68,69] demonstrated that the mono- and bilayer $PtSe_2$ are characterized with semiconductor band gaps in the intervals of 1.2−1.8 and 0.2−0.65 eV, respectively, while the structures from three layers to bulk are semimetallic (E_g = 0.12 eV). The calculated values for E_g in the present work are significantly larger than the expected values for optical band gap in this interval of thicknesses of thin-layer coatings. Similarly, higher band gap values in the case of thin $PtSe_2$ films in the range of 0.48−0.55 eV with thicknesses in the range of 6−8 nm are presented in ref 48. The reason for this effect can be assumed to be due to the polycrystalline microstructure of the thin films. Overlapping of the individual crystallites leads to the production of thin $PtSe_2$ films with significantly larger thicknesses and semiconducting properties.

3.4. Raman Analysis. Raman measurements were conducted on $PtSe_2$ with Pt deposition times of 3, 6, and 10 s and spectra labeled with the corresponding $PtSe_2$ thicknesses estimated by ellipsometry ($PtSe_2$-7, $PtSe_2$-9, and $PtSe_2$-12 nm, respectively) are shown in Figure 6a. The Raman analysis reveals typical A_{1g} and E_g vibrational modes, of which E_g represents an in-plane vibration of Se atoms while in the A_{1g} mode upper and lower Se atoms within each layer oscillate perpendicular to the layer plane. With increasing $PtSe_2$ film thickness, the E_g mode was found to red-shift due to the long-range Coulomb interactions and stacking-induced changes of the interlayer bonding.[7] On the other hand, as can be expected from its vibrational pattern, the relative intensity of the A_{1g} mode is known to increase for thicker $PtSe_2$ samples because of the enhanced interlayer van der Waals interaction in the presence of more monolayers.[70] There is also a prominent shoulder at 230−235 cm^{-1} resulting from an overlap of the A_{2u} and E_u longitudinal optical modes which are also sensitive to the $PtSe_2$ film thickness yielding more intense peaks for thinner samples.[70] This is also valid for our spectra in Figure 6a, which are presented normalized to the E_g intensity. For ($PtSe_2$-7 nm), the shoulder at 230−235 cm^{-1} is more strongly pronounced and almost twice as intense as that for the ($PtSe_2$-12 nm) sample. The thickness dependence of the E_g mode frequency and the A_{1g}/E_g peak intensity ratio is plotted in Figure 6b. The E_g mode frequency undergoes a shift from 177.7 cm^{-1} for ($PtSe_2$-7 nm) to 175.3 cm^{-1} for ($PtSe_2$-12 nm). As can also be appreciated from Figure 6b, in the same sequence, the peak intensity ratio of the lines A_{1g} and E_g increases slightly above unity. These results are in qualitative agreement with those established in a range of previous studies.[2,7,34,71] Still, our values of the A_{1g}/E_g peak intensity ratio point to slightly lower thicknesses for the three examined samples if the results of, e.g., ref 70 are taken as a base. However, as was shown recently, this ratio significantly depends on the c-axis orientation[71] and there are indications that it may also depend on the type of

https://doi.org/10.1021/acsomega.3c08235
ACS Omega 2024, 9, 14874−14886

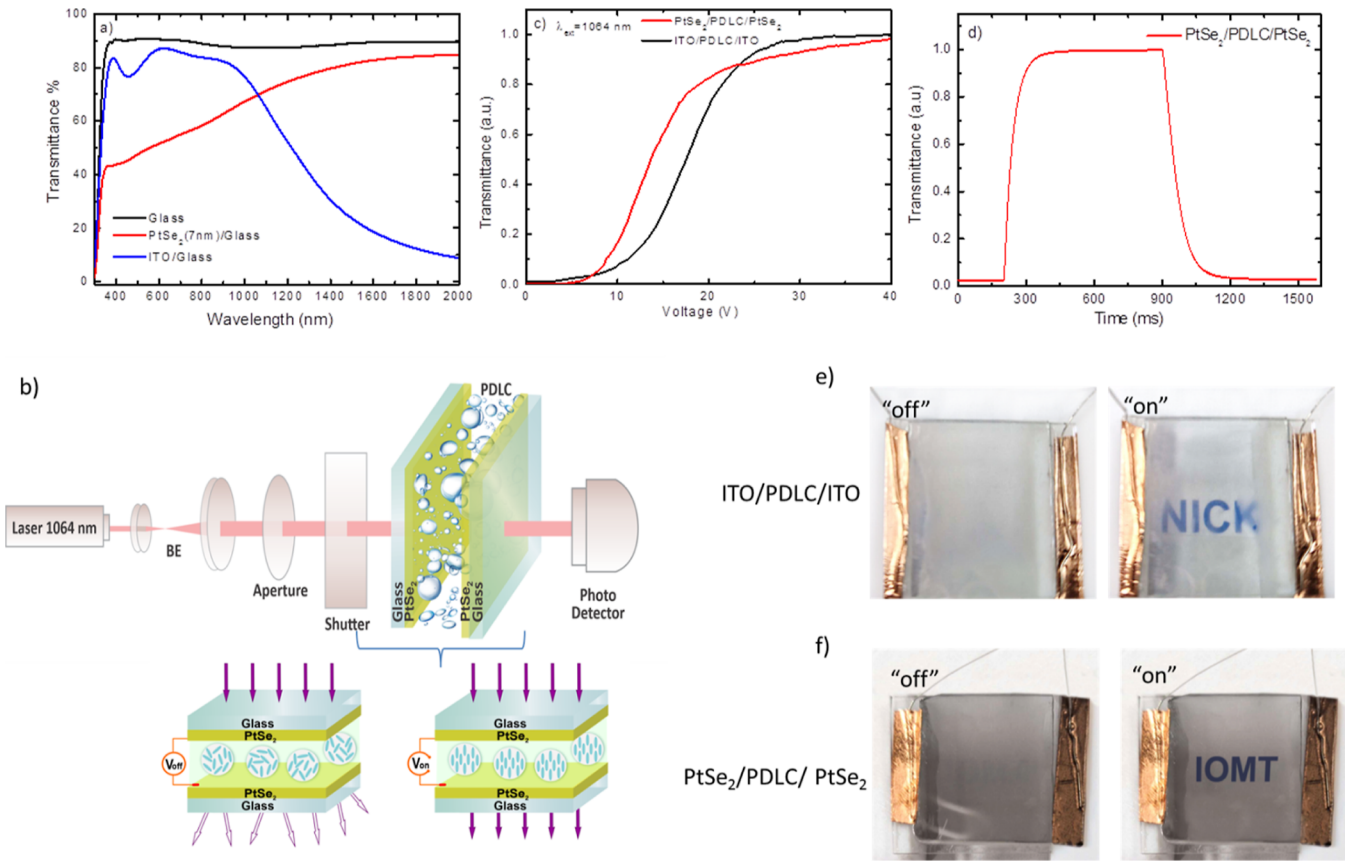

Figure 7. (a) Transmittance of $PtSe_2$ layer (7 nm)/glass at a near-infrared spectral range (spectra of commercially available ITO layer/glass is also shown for comparison); (b) experimental setup to measure electro-optical characteristics of assembled PDLC structures; (c) transmittance-voltage behavior of $PtSe_2$-based and ITO-based PDLC structures; (d) response time of $PtSe_2$-based PDLC structure; and (e,f) schematic diagram and photographs of "off "and "on" states of $PtSe_2$-based and ITO-based PDLC structures {video demonstration of both PDLC structures ["scattering" ("off") and ("transparent" ("on") states] are shown in Supporting Information, S4}.

substrates.[34] On the other hand, the TEM characterization (Figure 5f,i) indicates that in our samples both vertical and lateral stacking of the monolayers are present; thus, slight deviations from the results of other literature sources can be expected.

2D $PtSe_2$ possesses strong thickness dependence with regard to the optical constants n and k. This allows for the fine-tuning of these parameters and offers greater freedom when constructing devices for a specific application. Other TMDCs such as MoS_2 and WSe_2 do not share this property.[48] In optoelectronic devices, such as photodetectors and solar cells, these parameters could influence the efficiency and sensitivity of the device. A well-controlled band gap and peak transition energy can optimize the device for specific wavelengths.

3.5. Application of $PtSe_2$ as a Conductive Layer in PDLC Light Shutters Operating at a Near-Infrared Spectral Range. Based on the above performed characteristics and increased transmission tendency of $PtSe_2$ at a near-infrared spectral range (Figure 7a), the $PtSe_2$-7 nm sample has been selected as the transparent, conductive layer for making PDLC devices. Following the procedure of assembling the $PtSe_2$-based PDLC structure (Experimental section), first the cell was filled with an LC/monomer mixture and subsequently exposed with UV light (365 nm). As a result, randomly dispersed LC droplets were formed within the transparent polymer matrix and the structure appears opaque (scattering) due to the mismatch of the refractive indices between the LC molecules and the polymer matrix. It can turn to the transparent state under applied voltage which aligns the LC's nematic director to the direction of the electric field, allowing the light to pass through the cell. Figure 7b shows the experimental setup, together with the scattering and transparent sketch of the structure. Typical transmittance dependence of $PtSe_2$-based and ITO-based PDLC structures as a function of the applied voltage under a 1064 nm light exposure is shown in Figure 7c. Following the LC materials light modulation principles,[17] we defined the threshold voltage (V_{th}) as a value of the applied voltage necessary to reach 10% of the maximum transmittance, e.g., to "turn on" the PDLC cell ($V_{th\ (PtSe_2(7\ nm))} \sim 9$ V; $V_{th(ITO)} \sim 11$ V) and saturation voltage (V_{sat}) defined as the applied voltage value required to reach 90% of maximum transmittance T ($V_{sat\ (PtSe_2(7\ nm))} \sim 25.6$ V; $V_{sat\ (ITO)} \sim 24$ V). As seen from Figure 7b, the working characteristics of $PtSe_2$ (7 nm)-based PDLC surpassed the PDLC device made with ITO contacts, with lower threshold voltage required for the $PtSe_2$-based cell. Another recently used near-infrared transparent conductive material for making PDLC devices (instead ITO) is graphene,[72] however, it has the drawback of requirement to be transferred on large-scale substrates and to keep uniformity of the thickness, which is challenging. At the same time, $PtSe_2$ can be synthesized directly on glass substrates, which are commonly used substrates for PDLC devices. In addition, the response time and the fall time of the $PtSe_2$-based PDLC structure of 42 and

https://doi.org/10.1021/acsomega.3c08235
ACS Omega 2024, 9, 14874−14886

62 ms, respectively, were measured (Figure 7d). All the above electro-optical characteristics depend on the electrical conductivity of the supporting layers (the measured electrical conductivity of the $PtSe_2$ layer is presented at Table 1 and Supporting Information, S3) as well as of the LC droplet sizes, formed during the photopolymerization process in the polymer matrix.

Summarizing, we briefly demonstrated that intensity of the transmitted infrared light can be controlled by the application of an external voltage and the assembled $PtSe_2$-based PDLC structure can work as a near-infrared light shutter.

The proposed techniques open up a new perspective for $PtSe_2$ layer synthesis by the TAC approach at atmospheric pressure covering large area on inexpensive glass (soda lime) substrates that can be applied for near-infrared light shutters, smart solar heat structures, and further switchable optical devices for energy saving. Moreover, $PtSe_2$ can replace the commonly used ITO conductive layers not only due to ITO's limited sensitivity at a near-infrared spectral range but also due to the drawbacks of indium in nature (increasing production processing cost) and ceramic structure (brittleness), which limits applications in flexible and bendable structures and devices.

4. CONCLUSION

In summary, we have demonstrated low-temperature synthesis of uniform and homogeneous $PtSe_2$ nanolayers on inexpensive glass substrates using the atmospheric pressure TAC method. Ellipsometry measurements and calculations determine the thickness dependence based on the initial thickness of predeposited Pt layers (deposition time). XPS and Raman analyses prove the presence of 2D $PtSe_2$ layers and yield thickness estimates compatible with those determined by ellipsometry and AFM. The detailed TEM characterization reveals the polycrystalline nature of the layers and provides evidence for both vertical and lateral stackings of the monolayers within them. The phenomenon of anomalous dispersion of the refractive index can find applications in the design of optical filters, which can pass the shorter wavelengths and suppress the longer wavelengths. In addition, the application of transparent conductive $PtSe_2$ layers in PDLC structures that works as near-infrared light shutters makes $PtSe_2$ a promising candidate for implementation as a conductive layer for near-infrared ITO-free optoelectronic devices, smart windows, or energy-saving alternatives.

■ ASSOCIATED CONTENT

Supporting Information

The Supporting Information is available free of charge at https://pubs.acs.org/doi/10.1021/acsomega.3c08235.

SEM images of $PtSe_2$ layers; single semiconductor film with a rough overlayer on an absorbing substrate; electrical transport characteristics of $PtSe_2$; and video demonstration of $PtSe_2$-based and ITO-based PDLC structures (PDF)

■ AUTHOR INFORMATION

Corresponding Author

Vera Marinova − *Institute of Optical Materials and Technologies, Bulgarian Academy of Sciences, 1113 Sofia, Bulgaria; Department of Electrophysics, National Yang Ming Chiao Tung University, 30010 Hsinchu, Taiwan;* orcid.org/0000-0002-3499-0212; Email: vmarinova@iomt.bas.bg

Authors

Nikolay Minev − *Institute of Optical Materials and Technologies, Bulgarian Academy of Sciences, 1113 Sofia, Bulgaria*

Krastyo Buchkov − *Institute of Solid-State Physics, Bulgarian Academy of Sciences, 1784 Sofia, Bulgaria*

Nadia Todorova − *Institute of Nanoscience and Nanotechnology, National Centre for Scientific Research "Demokritos", 15341 Agia Paraskevi, Greece*

Rosen Todorov − *Institute of Optical Materials and Technologies, Bulgarian Academy of Sciences, 1113 Sofia, Bulgaria;* orcid.org/0000-0002-7674-1476

Vladimira Videva − *Institute of Optical Materials and Technologies, Bulgarian Academy of Sciences, 1113 Sofia, Bulgaria; Faculty of Chemistry and Pharmacy, Sofia University, 1164 Sofia, Bulgaria;* orcid.org/0000-0003-4695-8882

Maria Stefanova − *Institute of Optical Materials and Technologies, Bulgarian Academy of Sciences, 1113 Sofia, Bulgaria*

Peter Rafailov − *Institute of Solid-State Physics, Bulgarian Academy of Sciences, 1784 Sofia, Bulgaria*

Daniela Karashanova − *Institute of Optical Materials and Technologies, Bulgarian Academy of Sciences, 1113 Sofia, Bulgaria*

Hristosko Dikov − *Central Laboratory of Solar Energy and New Energy Sources, Bulgarian Academy of Sciences, 1784 Sofia, Bulgaria*

Velichka Strijkova − *Institute of Optical Materials and Technologies, Bulgarian Academy of Sciences, 1113 Sofia, Bulgaria*

Christos Trapalis − *Institute of Nanoscience and Nanotechnology, National Centre for Scientific Research "Demokritos", 15341 Agia Paraskevi, Greece*

Shiuan Huei Lin − *Department of Electrophysics, National Yang Ming Chiao Tung University, 30010 Hsinchu, Taiwan*

Dimitre Dimitrov − *Institute of Optical Materials and Technologies, Bulgarian Academy of Sciences, 1113 Sofia, Bulgaria; Institute of Solid-State Physics, Bulgarian Academy of Sciences, 1784 Sofia, Bulgaria*

Complete contact information is available at: https://pubs.acs.org/10.1021/acsomega.3c08235

Notes

The authors declare no competing financial interest.

■ ACKNOWLEDGMENTS

This work was funded by Bulgarian Science Fund under the project number DFNI KP-06-H-68/1. V.M., N.M., and P.R. acknowledge the financial support by the European Regional Development Fund within the Operational Programme "Science and Education for Smart Growth 2014−2020" under the Project CoE 'National Center of Mechatronics and Clean Technologies' BG05M2OP001-1.001-0008-C01. Research equipment of distributed research infrastructure INFRAMAT (part of Bulgarian National roadmap for research infrastructures) supported by Bulgarian Ministry of Education and Science is also acknowledged. We are grateful to bilateral grant agreement between Bulgarian Academy of Sciences

https://doi.org/10.1021/acsomega.3c08235
ACS Omega 2024, 9, 14874−14886

(BAS), Bulgaria and NSTC, Taiwan under PPP project NSTC 113-2927-I-A49-507 by IOMT-BAS and NYCU, Taiwan.

REFERENCES

(1) Yim, C.; Lee, K.; McEvoy, N.; O'Brien, M.; Riazimehr, S.; Berner, N. C.; Cullen, C. P.; Kotakoski, J.; Meyer, J. C.; Lemme, M. C.; Duesberg, G. S. High-Performance Hybrid Electronic Devices from Layered $PtSe_2$ Films Grown at Low Temperature. *ACS Nano* **2016**, *10* (10), 9550−9558.

(2) Kim, J. H.; Youn, S.; Go, T. W.; Kim, J.; Yoo, C.; Shawkat, M. S.; Han, S. S.; Jeon, S. j.; Jung, Y.; Park, J. Y.; Lee, W. Revealing Pt-Seed-Induced Structural Effects to Tribological/Electrical/Thermoelectric Modulations in Two-Dimensional $PtSe_2$ Using Scanning Probe Microscopy. *Nano Energy* **2022**, *91* (November2021), 106693.

(3) Chung, C. C.; Yeh, H.; Wu, P. H.; Lin, C. C.; Li, C. S.; Yeh, T. T.; Chou, Y.; Wei, C. Y.; Wen, C. Y.; Chou, Y. C.; Luo, C. W.; Wu, C. I.; Li, M. Y.; Li, L. J.; Chang, W. H.; Chen, C. W. Atomic-Layer Controlled Interfacial Band Engineering at Two-Dimensional Layered $PtSe_2$/Si Heterojunctions for Efficient Photoelectrochemical Hydrogen Production. *ACS Nano* **2021**, *15* (3), 4627−4635.

(4) Chen, E.; Xu, W.; Chen, J.; Warner, J. H. 2D Layered Noble Metal Dichalcogenides (Pt, Pd, Se, S) for Electronics and Energy Applications. *Mater. Today Adv.* **2020**, *7*, 100076.

(5) Song, L.; Li, H.; Zhang, Y.; Shi, J. Recent Progress of Two-Dimensional Metallic Transition Metal Dichalcogenides: Syntheses, Physical Properties, and Applications. *J. Appl. Phys.* **2022**, *131* (6), 060902.

(6) Wang, G.; Wang, Z.; McEvoy, N.; Fan, P.; Blau, W. J. Layered $PtSe_2$ for Sensing, Photonic, and (Opto-)Electronic Applications. *Adv. Mater.* **2021**, *33* (1), 1−23.

(7) Jiang, W.; Wang, X.; Chen, Y.; Wu, G.; Ba, K.; Xuan, N.; Sun, Y.; Gong, P.; Bao, J.; Shen, H.; Lin, T.; Meng, X.; Wang, J.; Sun, Z. Large-Area High Quality $PtSe_2$ Thin Film with Versatile Polarity. *InfoMat* **2019**, *1* (2), 260−267.

(8) Zhou, J.; Kong, X.; Sekhar, M. C.; Lin, J.; Le Goualher, F.; Xu, R.; Wang, X.; Chen, Y.; Zhou, Y.; Zhu, C.; Lu, W.; Liu, F.; Tang, B.; Guo, Z.; Zhu, C.; Cheng, Z.; Yu, T.; Suenaga, K.; Sun, D.; Ji, W.; Liu, Z. Epitaxial Synthesis of Monolayer $PtSe_2$ Single Crystal on $MoSe_2$ with Strong Interlayer Coupling. *ACS Nano* **2019**, *13* (10), 10929−10938.

(9) Wang, Y.; Li, L.; Yao, W.; Song, S.; Sun, J. T.; Pan, J.; Ren, X.; Li, C.; Okunishi, E.; Wang, Y.-Q.; Wang, E.; Shao, Y.; Zhang, Y. Y.; Yang, H.; Schwier, E. F.; Iwasawa, H.; Shimada, K.; Taniguchi, M.; Cheng, Z.; Zhou, S.; Du, S.; Pennycook, S. J.; Pantelides, S. T.; Gao, H.-J. Monolayer $PtSe_2$, a New Semiconducting Transition-Metal-Dichalcogenide, Epitaxially Grown by Direct Selenization of Pt. *Nano Lett.* **2015**, *15* (6), 4013−4018.

(10) Shawkat, M. S.; Gil, J.; Han, S. S.; Ko, T.-J.; Wang, M.; Dev, D.; Kwon, J.; Lee, G.-H.; Oh, K. H.; Chung, H.-S.; Roy, T.; Jung, Y.; Jung, Y. Thickness-Independent Semiconducting-to-Metallic Conversion in Wafer-Scale Two-Dimensional $PtSe_2$ Layers by Plasma-Driven Chalcogen Defect Engineering. *ACS Appl. Mater. Interfaces* **2020**, *12* (12), 14341−14351.

(11) Gong, Y.; Lin, Z.; Chen, Y. X.; Khan, Q.; Wang, C.; Zhang, B.; Nie, G.; Xie, N.; Li, D. Two-Dimensional Platinum Diselenide: Synthesis, Emerging Applications, and Future Challenges. *Nano-Micro Letters*; Springer, 2020; pp 1−34.

(12) Kireev, D.; Okogbue, E.; Jayanth, R.; Ko, T.-J.; Jung, Y.; Akinwande, D. Multipurpose and Reusable Ultrathin Electronic Tattoos Based on $PtSe_2$ and $PtTe_2$. *ACS Nano* **2021**, *15* (2), 2800−2811.

(13) Wu, M.; Shi, Y.; Li, R.; Wang, P. Spectrally Selective Smart Window with High Near-Infrared Light Shielding and Controllable Visible Light Transmittance. *ACS Appl. Mater. Interfaces* **2018**, *10* (46), 39819−39827.

(14) Zhang, R.; Zhang, Z.; Han, J.; Yang, L.; li, J.; Song, Z.; Wang, T.; Zhu, J. Advanced Liquid Crystal-Based Switchable Optical Devices for Light Protection Applications: Principles and Strategies. *Light Sci. Appl.* **2023**, *12* (1), 11.

(15) Shen, W.; Li, G. Recent Progress in Liquid Crystal-Based Smart Windows: Materials, Structures, and Design. *Laser Photon. Rev.* **2023**, *17* (1), 2200207.

(16) Wang, Y.; Zhang, Z.; Xiao, S.; Tsang, H. K. Two-Dimensional Layered $PtSe_2$ for High Speed Near-Infrared Electro-Optic Modulation. *Eur. Conf. Integr. Opt.* **2023**, *1* (April), 19−21.

(17) Yeh, P.; Gu, C. *Optics of Liquid Crystal Displays*; Wiley, 2009; Vol. *67*, p 792.

(18) Gatensby, R.; McEvoy, N.; Lee, K.; Hallam, T.; Berner, N. C.; Rezvani, E.; Winters, S.; O'Brien, M.; Duesberg, G. S. Controlled Synthesis of Transition Metal Dichalcogenide Thin Films for Electronic Applications. *Appl. Surf. Sci.* **2014**, *297*, 139−146.

(19) Gatensby, R.; Hallam, T.; Lee, K.; McEvoy, N.; Duesberg, G. S. Investigations of Vapour-Phase Deposited Transition Metal Dichalcogenide Films for Future Electronic Applications. *Solid State Electron.* **2016**, *125*, 39−51.

(20) McManus, J. B.; Cunningham, G.; McEvoy, N.; Cullen, C. P.; Gity, F.; Schmidt, M.; McAteer, D.; Mullarkey, D.; Shvets, I. V.; Hurley, P. K.; Hallam, T.; Duesberg, G. S. Growth of 1T′ $MoTe_2$ by Thermally Assisted Conversion of Electrodeposited Tellurium Films. *ACS Appl. Energy Mater.* **2019**, *2* (1), 521−530.

(21) He, J.; Jiang, W.; Zhu, X.; Zhang, R.; Wang, J.; Zhu, M.; Wang, S.; Zheng, Y.; Chen, L. Optical Properties of Thickness-Controlled $PtSe_2$ Thin Films Studied via Spectroscopic Ellipsometry. *Phys. Chem. Chem. Phys.* **2020**, *22* (45), 26383−26389.

(22) Zhou, K.; Shen, J.; Li, X.; Hong, X.; Feng, W.; Tang, X.; Jiang, X.; Wei, D.; Chen, Y.; Liu, X.; Xie, Y.; Wei, D.; Sun, T. Broadband Photodetector Based on 2D Layered $PtSe_2$/Silicon Heterojunction at Room-Temperature. *Phys. E Low-dimens. Syst. Nanostruct.* **2020**, *123*, 114147.

(23) Shi, J.; Huan, Y.; Hong, M.; Xu, R.; Yang, P.; Zhang, Z.; Zou, X.; Zhang, Y. Chemical Vapor Deposition Grown Large-Scale Atomically Thin Platinum Diselenide with Semimetal-Semiconductor Transition. *ACS Nano* **2019**, *13* (7), 8442−8451.

(24) Yu, X.; Yu, P.; Wu, D.; Singh, B.; Zeng, Q.; Lin, H.; Zhou, W.; Lin, J.; Suenaga, K.; Liu, Z.; Wang, Q. J. Atomically Thin Noble Metal Dichalcogenide: A Broadband Mid-Infrared Semiconductor. *Nat. Commun.* **2018**, *9* (1), 1545.

(25) Xie, C.; Zeng, L.; Zhang, Z.; Tsang, Y. H.; Luo, L.; Lee, J. H. High-Performance Broadband Heterojunction Photodetectors Based on Multilayered $PtSe_2$ Directly Grown on a Si Substrate. *Nanoscale* **2018**, *10* (32), 15285−15293.

(26) Shawkat, M. S.; Chung, H. S.; Dev, D.; Das, S.; Roy, T.; Jung, Y. Two-Dimensional/Three-Dimensional Schottky Junction Photovoltaic Devices Realized by the Direct CVD Growth of VdW 2D $PtSe_2$ Layers on Silicon. *ACS Appl. Mater. Interfaces* **2019**, *11* (30), 27251−27258.

(27) Yim, C.; McEvoy, N.; Riazimehr, S.; Schneider, D. S.; Gity, F.; Monaghan, S.; Hurley, P. K.; Lemme, M. C.; Duesberg, G. S. Wide Spectral Photoresponse of Layered Platinum Diselenide-Based Photodiodes. *Nano Lett.* **2018**, *18* (3), 1794−1800.

(28) Tao, L.; Huang, X.; He, J.; Lou, Y.; Zeng, L.; Li, Y.; Long, H.; Li, J.; Zhang, L.; Tsang, Y. H. Vertically Standing $PtSe_2$ Film: A Saturable Absorber for a Passively Mode-Locked Nd:$LuVO_4$ Laser. *Photon. Res.* **2018**, *6* (7), 750.

(29) Wang, G.; Wang, K.; McEvoy, N.; Bai, Z.; Cullen, C. P.; Murphy, C. N.; McManus, J. B.; Magan, J. J.; Smith, C. M.; Duesberg, G. S.; Kaminer, I.; Wang, J.; Blau, W. J. Ultrafast Carrier Dynamics and Bandgap Renormalization in Layered $PtSe_2$. *Small* **2019**, *15* (34), 1−9.

(30) Wang, L.; Zhang, S.; McEvoy, N.; Sun, Y.; Huang, J.; Xie, Y.; Dong, N.; Zhang, X.; Kislyakov, I. M.; Nunzi, J. M.; Zhang, L.; Wang, J. Nonlinear Optical Signatures of the Transition from Semiconductor to Semimetal in $PtSe_2$. *Laser Photon. Rev.* **2019**, *13* (8), 1−13.

(31) He, J.; Li, Y.; Lou, Y.; Zeng, G.; Tao, L. Optical Deposition of $PtSe_2$ on Fiber End Face for Yb-Doped Mode-Locked Fiber Laser. *Optik* **2019**, *198* (August), 163298.

https://doi.org/10.1021/acsomega.3c08235
ACS Omega 2024, 9, 14874−14886

(32) Li, Z.; Li, R.; Pang, C.; Dong, N.; Wang, J.; Yu, H.; Chen, F. 88 GHz Q-Switched Mode-Locked Waveguide Lasers Modulated by $PtSe_2$ Saturable Absorber. *Opt. Express* **2019**, *27* (6), 8727.
(33) Zhuo, R.; Zeng, L.; Yuan, H.; Wu, D.; Wang, Y.; Shi, Z.; Xu, T.; Tian, Y.; Li, X.; Tsang, Y. H. In-Situ Fabrication of $PtSe_2$/GaN Heterojunction for Self-Powered Deep Ultraviolet Photodetector with Ultrahigh Current on/off Ratio and Detectivity. *Nano Res.* **2019**, *12* (1), 183−189.
(34) Zhang, K.; Wang, M.; Zhou, X.; Wang, Y.; Shen, S.; Deng, K.; Peng, H.; Li, J.; Lai, X.; Zhang, L.; Wu, Y.; Duan, W.; Yu, P.; Zhou, S. Growth of Large Scale PtTe, $PtTe_2$ and $PtSe_2$ Films on a Wide Range of Substrates. *Nano Res.* **2021**, *14* (6), 1663−1667.
(35) Okogbue, E.; Han, S. S.; Ko, T.-J.; Chung, H.-S.; Ma, J.; Shawkat, M. S.; Kim, J. H.; Kim, J. H.; Ji, E.; Oh, K. H.; Zhai, L.; Lee, G.-H.; Jung, Y. Multifunctional Two-Dimensional $PtSe_2$-Layer Kirigami Conductors with 2000% Stretchability and Metallic-to-Semiconducting Tunability. *Nano Lett.* **2019**, *19* (11), 7598−7607.
(36) Wang, D.; Zhou, Y.; Zhang, H.; Zhang, R.; Dong, H.; Xu, R.; Cheng, Z.; He, Y.; Wang, Z. Wafer-Scale Growth of Pristine and Doped Monolayer MoS_2 Films for Electronic Device Applications. *Inorg. Chem.* **2020**, *59* (23), 17356−17363.
(37) Tai, G.; Zeng, T.; Yu, J.; Zhou, J.; You, Y.; Wang, X.; Wu, H.; Sun, X.; Hu, T.; Guo, W. Fast and Large-Area Growth of Uniform MoS_2 Monolayers on Molybdenum Foils. *Nanoscale* **2016**, *8* (4), 2234−2241.
(38) Song, H. J.; Son, M.; Park, C.; Lim, H.; Levendorf, M. P.; Tsen, A. W.; Park, J.; Choi, H. C. Large Scale Metal-Free Synthesis of Graphene on Sapphire and Transfer-Free Device Fabrication. *Nanoscale* **2012**, *4* (10), 3050.
(39) Shan, J.; Sun, J.; Liu, Z. Chemical Vapor Deposition Synthesis of Graphene over Sapphire Substrates. *ChemNanoMat* **2021**, *7* (5), 515−525.
(40) Wu, Z.; Tai, G.; Liu, R.; Hou, C.; Shao, W.; Liang, X.; Wu, Z. Van Der Waals Epitaxial Growth of Borophene on a Mica Substrate toward a High-Performance Photodetector. *ACS Appl. Mater. Interfaces* **2021**, *13* (27), 31808−31815.
(41) Han, S. S.; Kim, J. H.; Noh, C.; Kim, J. H.; Ji, E.; Kwon, J.; Yu, S. M.; Ko, T. J.; Okogbue, E.; Oh, K. H.; Chung, H. S.; Jung, Y.; Lee, G. H.; Jung, Y. Horizontal-to-Vertical Transition of 2D Layer Orientation in Low-Temperature Chemical Vapor Deposition-Grown $PtSe_2$ and Its Influences on Electrical Properties and Device Applications. *ACS Appl. Mater. Interfaces* **2019**, *11* (14), 13598−13607.
(42) Sedky, S.; Witvrouw, A.; Bender, H.; Baert, K. Experimental Determination of the Maximum Post-Process Annealing Temperature for Standard CMOS Wafers. *IEEE Trans. Electron Devices* **2001**, *48* (2), 377−385.
(43) Todorova, N.; Minev, N.; Marinova, V.; Buchkov, K.; Videva, V.; Todorov, R.; Rafailov, P.; Strijkova, V.; Psycharis, V.; Giannakopoulou, T.; Papailias, I.; Ioannidis, N.; Mitrikas, G.; Dimitrov, D.; Trapalis, C. Two-Dimensional $PtSe_2$ Coatings with Antibacterial Activity. *Appl. Surf. Sci.* **2023**, *611*, 155534.
(44) Lin, S.; Liu, Y.; Hu, Z.; Lu, W.; Mak, C. H.; Zeng, L.; Zhao, J.; Li, Y.; Yan, F.; Tsang, Y. H.; Zhang, X.; Lau, S. P. Tunable Active Edge Sites in $PtSe_2$ Films towards Hydrogen Evolution Reaction. *Nano Energy* **2017**, *42*, 26−33.
(45) Kim, H.-S.; Jeong, J.; Kwon, G.-H.; Park, S.; Jeong, K.; Choi, Y.-H.; Kwon, H.; Baik, M.; Im, S.; Cho, M.-H. Ultrathin Platinum Diselenide Synthesis Controlling Initial Growth Kinetics: Interfacial Reaction Depending on Thickness and Substrate. *Appl. Surf. Sci.* **2021**, *564*, 150300.
(46) Dionisiev, I.; Marinova, V.; Buchkov, K.; Dikov, H.; Avramova, I.; Dimitrov, D. Synthesis and Characterizations of 2D Platinum Diselenide. In *2nd Coatings and Interfaces Web Conference (CIWC-2 2020)*; MDPI: Basel Switzerland, 2020, p 22.
(47) Xu, H.; Zhang, H.; Liu, Y.; Zhang, S.; Sun, Y.; Guo, Z.; Sheng, Y.; Wang, X.; Luo, C.; Wu, X.; Wang, J.; Hu, W.; Xu, Z.; Sun, Q.; Zhou, P.; Shi, J.; Sun, Z.; Zhang, D. W.; Bao, W. Controlled Doping of Wafer-Scale $PtSe_2$ Films for Device Application. *Adv. Funct. Mater.* **2019**, *29* (4), 1805614.
(48) Xie, J.; Zhang, D.; Yan, X.-Q.; Ren, M.; Zhao, X.; Liu, F.; Sun, R.; Li, X.; Li, Z.; Chen, S.; Liu, Z.-B.; Tian, J.-G. Optical Properties of Chemical Vapor Deposition-Grown $PtSe_2$ Characterized by Spectroscopic Ellipsometry. *2D Mater.* **2019**, *6* (3), 035011.
(49) Chang, Y.; Zhai, P.; Hou, J.; Zhao, J.; Gao, J. Excellent HER and OER Catalyzing Performance of Se-Vacancies in Defects-Engineered $PtSe_2$: From Simulation to Experiment. *Adv. Energy Mater.* **2022**, *12* (1), 2102359.
(50) Wang, Z.; Dong, M. Cutting Edge Materials of Two-Dimensional Platinum Diselenide. *ACS Symp. Ser.* **2020**, *1353*, 317−345.
(51) Ma, H.; Qian, Q.; Qin, B.; Wan, Z.; Wu, R.; Zhao, B.; Zhang, H.; Zhang, Z.; Li, J.; Zhang, Z.; Li, B.; Wang, L.; Duan, X. Controlled Synthesis of Ultrathin $PtSe_2$ Nanosheets with Thickness-Tunable Electrical and Magnetoelectrical Properties. *Adv. Sci.* **2022**, *9* (1), 2103507.
(52) Wang, Z.; Xie, Y.; Wang, H.; Wu, R.; Nan, T.; Zhan, Y.; Sun, J.; Jiang, T.; Zhao, Y.; Lei, Y.; Yang, M.; Wang, W.; Zhu, Q.; Ma, X.; Hao, Y. NaCl-Assisted One-Step Growth of MoS_2-WS_2 in-Plane Heterostructures. *Nanotechnology* **2017**, *28* (32), 325602.
(53) Paz, Y.; Heller, A. Photo-Oxidatively Self-Cleaning Transparent Titanium Dioxide Films on Soda Lime Glass: The Deleterious Effect of Sodium Contamination and Its Prevention. *J. Mater. Res.* **1997**, *12* (10), 2759−2766.
(54) Morales, C.; Flores, E.; Yoda, S.; Niño, M.; Martín y Marero, D.; Soriano, L.; Rojo, J.; Ares, J. R.; Ferrer, I. J.; Sánchez, C. An XPS Investigation on the Influence of the Substrate and Growth Conditions on Pyrite Thin Films Surface Composition. *Appl. Surf. Sci.* **2019**, *492*, 651−660.
(55) Yoon, J.; Seong, T.; Jeong, J. Effect of a Mo Back Contact on Na Diffusion in CIGS Thin Film Solar Cells. *Prog. Photovoltaics Res. Appl.* **2013**, *21* (1), 58−63.
(56) Niles, D. W.; Ramanathan, K.; Hasoon, F.; Noufi, R.; Tielsch, B. J.; Fulghum, J. E. Na Impurity Chemistry in Photovoltaic CIGS Thin Films: Investigation with x-Ray Photoelectron Spectroscopy. *J. Vac. Sci. Technol., A* **1997**, *15* (6), 3044−3049.
(57) Erslev, P. T.; Lee, J. W.; Shafarman, W. N.; Cohen, J. D. The Influence of Na on Metastable Defect Kinetics in CIGS Materials. *Thin Solid Films* **2009**, *517* (7), 2277−2281.
(58) Wei, S.-H.; Zhang, S. B.; Zunger, A. Effects of Na on the Electrical and Structural Properties of $CuInSe_2$. *J. Appl. Phys.* **1999**, *85* (10), 7214−7218.
(59) Giannakopoulou, T.; Todorova, N.; Trapalis, C.; Vaimakis, T. Effect of Fluorine Doping and SiO_2 Under-Layer on the Optical Properties of TiO2 Thin Films. *Mater. Lett.* **2007**, *61* (23−24), 4474−4477.
(60) Pribusová Slušná, L.; Vojteková, T.; Hrdá, J.; Pálková, H.; Siffalovic, P.; Sojková, M.; Végsö, K.; Hutár, P.; Dobročka, E.; Varga, M.; Hulman, M. Optical Characterization of Few-Layer $PtSe_2$ Nanosheet Films. *ACS Omega* **2021**, *6* (51), 35398−35403.
(61) Ermolaev, G. A.; Voronin, K. V.; Tatmyshevskiy, M. K.; Mazitov, A. B.; Slavich, A. S.; Yakubovsky, D. I.; Tselin, A. P.; Mironov, M. S.; Romanov, R. I.; Markeev, A. M.; Kruglov, I. A.; Novikov, S. M.; Vyshnevyy, A. A.; Arsenin, A. V.; Volkov, V. S. Broadband Optical Properties of Atomically Thin PtS_2 and $PtSe_2$. *Nanomaterials* **2021**, *11* (12), 3269.
(62) Jellison, G. E.; Modine, F. A. Parameterization of the Optical Functions of Amorphous Materials in the Interband Region. *Appl. Phys. Lett.* **1996**, *69* (3), 371−373.
(63) Redinger, A.; Siebentritt, S. Loss Mechanisms in Kesterite Solar Cells. *Copper Zinc Tin Sulfide-Based Thin-Film Sol. Cells* **2014**, *627*, 363−386.
(64) Yu, Y.; Yu, Y.; Cai, Y.; Li, W.; Gurarslan, A.; Peelaers, H.; Aspnes, D. E.; Van De Walle, C. G.; Nguyen, N. V.; Zhang, Y. W.; Cao, L. Exciton-Dominated Dielectric Function of Atomically Thin MoS_2 Films. *Sci. Rep.* **2015**, *5*, 16996.

https://doi.org/10.1021/acsomega.3c08235
ACS Omega 2024, 9, 14874−14886

(65) Sajjad, M.; Singh, N.; Schwingenschlögl, U. Strongly Bound Excitons in Monolayer PtS_2 and $PtSe_2$. *Appl. Phys. Lett.* **2018**, *112* (4), 043101.
(66) Zhussupbekov, K.; Cullen, C. P.; Zhussupbekova, A.; Shvets, I. V.; Duesberg, G. S.; McEvoy, N.; Ó Coileáin, C. Electronic and Structural Characterisation of Polycrystalline Platinum Disulfide Thin Films. *RSC Adv.* **2020**, *10* (69), 42001−42007.
(67) Su, T. Y.; Chen, Y. Z.; Wang, Y. C.; Tang, S. Y.; Shih, Y. C.; Cheng, F.; Wang, Z. M.; Lin, H. N.; Chueh, Y. L. Highly Sensitive, Selective and Stable NO_2 Gas Sensors with a Ppb-Level Detection Limit on 2D-Platinum Diselenide Films. *J. Mater. Chem. C* **2020**, *8* (14), 4851−4858.
(68) Villaos, R. A. B.; Crisostomo, C. P.; Huang, Z. Q.; Huang, S. M.; Padama, A. A. B.; Albao, M. A.; Lin, H.; Chuang, F. C. Thickness Dependent Electronic Properties of Pt Dichalcogenides. *npj 2D Mater. Appl.* **2019**, *3* (1), 2−8.
(69) Li, J.; Kolekar, S.; Ghorbani-Asl, M.; Lehnert, T.; Biskupek, J.; Kaiser, U.; Krasheninnikov, A. V.; Batzill, M. Layer-Dependent Band Gaps of Platinum Dichalcogenides. *ACS Nano* **2021**, *15* (8), 13249−13259.
(70) O'Brien, M.; McEvoy, N.; Motta, C.; Zheng, J.-Y.; Berner, N. C.; Kotakoski, J.; Elibol, K.; Pennycook, T. J.; Meyer, J. C.; Yim, C.; Abid, M.; Hallam, T.; Donegan, J. F.; Sanvito, S.; Duesberg, G. S. Raman Characterization of Platinum Diselenide Thin Films. *2D Mater.* **2016**, *3* (2), 021004.
(71) Kozak, A.; Sojkova, M.; Gucmann, F.; Bodík, M.; Végso, K.; Dobrocka, E.; Píš, I.; Bondino, F.; Hulman, M.; Šiffalovič, P.; Ťapajna, M. Effect of the Crystallographic C-Axis Orientation on the Tribological Properties of the Few-Layer $PtSe_2$. *Appl. Surf. Sci.* **2022**, *605*, 154883.
(72) Kim, E. M.; Kim, S. J.; Choi, G. B.; Lee, J.; Koo, M. M.; Kim, J.; Kim, Y. W.; Lee, J.; Kim, J. H.; Seo, T. H. A Graphene-Based Polymer-Dispersed Liquid Crystal Device Enabled through a Water-Induced Interface Cleaning Process. *Nanomaterials* **2023**, *13* (16), 2309.

https://doi.org/10.1021/acsomega.3c08235
ACS Omega 2024, 9, 14874−14886